Journal of Sound and Vibration (1998) **211**(4), 571–592

MODELLING, SYNTHESIS AND DYNAMIC ANALYSIS OF COMPLEX FLEXIBLE ROTOR SYSTEMS

H. FANG AND B. YANG

Department of Mechanical Engineering, University of Southern California, Los Angeles, CA 90089-1453, *U.S.A.*

(*Received* 17 *February* 1997, *and in final form* 7 *October* 1997)

A distributed transfer function synthesis is developed for modelling and analysis of rotor systems assembled from multiple flexible and rigid components. The method delivers highly accurate and closed-form analytical solutions, and is capable of treating non-self-adjoint effects, general boundary conditions and multi-body coupling. It is shown that the proposed method provides a useful analysis tool for many problems in rotor dynamics.

1. INTRODUCTION

Complex rotor systems have broad industrial applications, such as steam and gas turbines, turbogenerators, reciprocating and centrifugal compressors, internal combustion engines, and grinding and milling machines. Flexible rotating shafts are employed in those machines for efficient power transmission, high speed transportation, or cost-effective operation. The vibration of those flexible components is therefore a major concern in optimal design of complex rotor systems.

The vibration of flexible rotating shafts has been extensively studied in the past [1–8]. Various numerical methods of analysis have been developed, including the Rayleigh–Ritz method [4], direct stiffness method [6], assumed modes method [9], Galerkin method [10, 11], modal synthesis method [12], transfer matrix method [5, 8], and finite element methods [13–15]. Parallel to numerical methods, analytical techniques have also been developed by many researchers. The classical boundary value method is applied to study the natural frequencies and normal modes of rotating Timoshenko beams [16, 17], and the critical speeds of rotating flexible shafts [18, 19]. A generalized modal analysis based on a state–space formulation provides the closed-form transient response of a rotating flexible shaft under various excitations [20]. A generalized displacement method is adopted to estimate the eigensolutions of a rotating stepped beam [21]. Transfer matrix analysis using distributed elements yields the steady state response of stepped flexible rotors [5], and a rotating Timoshenko beam carrying rigid thin disks [22].

Although the finite element method has been a standard structural analysis tool, analytical methods are always desirable because they deliver accurate results, are numerically efficient, and provide deep physical insight into the problem. This is especially true for rotor systems with extremely flexible rotating shafts, as has been noted by many researchers [1, 3, 5, 7]. However, most analytical methods are only valid for fairly simple rotor systems. Exact and closed-form analytical solutions for multi-body, branched flexible rotor systems are not available.

0022–460X/98/140571 + 22 $25.00/0/sv971346

The objective of this study is to develop a closed-form analytical solution method, namely the Distributed Transfer Function Synthesis (DTFS), for accurate modelling and dynamic analysis of complex flexible rotor systems. The concept of distributed transfer functions was introduced by Butkoviskiy [23], and has been applied to non-rotating flexible structures [24, 25]. The current investigation is not a simple extension of the previous distributed transfer function modelling; it deals with several practical and difficult issues in rotor dynamics, including non-self-adjoint effects of gyroscopic, damping and circulatory forces, coupling of rotating flexible shafts and lumped components, unbalanced masses, whirling motion, critical speeds, and anisotropic bearings/supports. These issues distinguish the modelling and analysis of a complex flexible rotor system from that of a non-rotating structure, and have limited the utility of many conventional solution methods. Obviously, the development of a closed-form analytical method for complex flexible rotor systems is not a trivial task.

The proposed DTFS is unique in that it combines the high accuracy of analytical solutions, and the versatility of finite element analysis in treating multi-body coupling and general boundary conditions. For instance, consider the hypothetic rotor system in Figure 1, which is an assembly of multiple flexible rotating shafts with mounted rigid disks, constrained by bearings, and coupled by gears and inter-shaft bearings. In the DTFS, the rotor system is first decomposed into a number of distributed and lumped components by nodes at which the components are inter-connected. The response of each flexible shaft component is then expressed by exact and closed-form distributed transfer functions in terms of its nodal displacement parameters. As such, a multi-body, branched rotor system is conveniently assembled from these components by imposing force balance at the nodes, leading to a global dynamic equilibrium equation. Solution of the dynamic equilibrium equation yields accurate prediction of the system response at every point.

The DTFS is different from existing methods in several aspects. First, without discretization or approximation, the DTFS delivers exact and closed-form solutions for a large class of complex flexible rotor systems. Second, unlike standard series solution methods, the DTFS does not need to select specific comparison or admissible functions for particular boundary conditions and shaft models. Third, compared to the transfer matrix method, the DTFS is more convenient in dealing with multi-body and branched structures, and avoids the difficulty in determining transfer matrices for systems with non-self-adjoint gyroscopic, damping and circulatory forces. Additionally, the DTFS-based analysis involves a minimum number of unknowns because a flexible shaft component is not to be further divided into smaller elements. These features make the proposed method attractive and practical in engineering analysis.

The remainder of the paper is arranged as follows. The transfer function modelling of distributed and lumped components is given in section 2 and the distributed transfer function synthesis is presented in section 3. The DTFS is applied to various dynamic problems in section 4, and illustrated by three numerical examples in section 5.

2. MODELLING OF DISTRIBUTED AND LUMPED COMPONENTS

A complex rotor system is composed of multiple distributed and lumped components such as flexible rotating shafts, rigid disks, bearings, and gears; see Figure 1. In this section, these components are modelled by transfer functions in the Laplace transform domain.

2.1. UNIFORM FLEXIBLE ROTATING SHAFT

For the uniform flexible rotating shaft in Figure 2, its transverse displacements $u(z, t)$

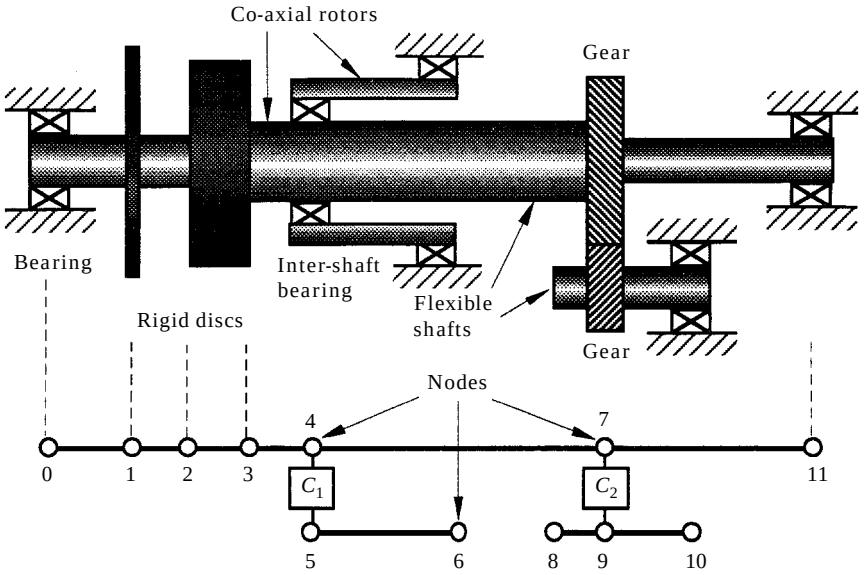

Figure 1. A hypothetic complex rotor system: C_1—coupling of nodes 4 and 5 by the inter-shaft bearing; C_2—coupling of nodes 7 and 9 by the gear pair.

and $v(z, t)$ described in a fixed co-ordinate system $oxyz$ are governed by the partial differential equations

$$EI\frac{\partial^4 u(z,t)}{\partial z^4} - 2\rho I\Omega\frac{\partial^3 v(z,t)}{\partial z^2\,\partial t} - \rho I\frac{\partial^4 u(z,t)}{\partial z^2\,\partial t^2} + \rho A\frac{\partial^2 u(z,t)}{\partial t^2} = f_x(z,t), \tag{1a}$$

$$EI\frac{\partial^4 v(z,t)}{\partial z^4} + 2\rho I\Omega\frac{\partial^3 u(z,t)}{\partial z^2\,\partial t} - \rho I\frac{\partial^4 v(z,t)}{\partial z^2\,\partial t^2} + \rho A\frac{\partial^2 v(z,t)}{\partial t^2} = f_y(z,t), \qquad 0 \leqslant z \leqslant L, \tag{1b}$$

with arbitrary boundary conditions specified at its two ends, nodes i and j. Here ρ, E, A, I and Ω are the density, Young's modulus, cross-section area, moment of inertia and rotation speed of the shaft, respectively, and $f_x(z, t)$ and $f_y(z, t)$ are the external forces. The internal shear forces and bending moments of the component are given by [26]

$$F_x(z,t) = -\rho I\frac{\partial^3 u(z,t)}{\partial z\,\partial t^2} - 2\rho I\Omega\frac{\partial^2 v(z,t)}{\partial z\,\partial t} + EI\frac{\partial^3 u(z,t)}{\partial z^3}, \tag{2a}$$

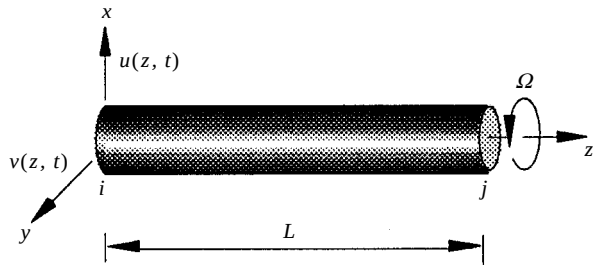

Figure 2. A uniform flexible rotating shaft.

$$F_y(z,t) = -\rho I \frac{\partial^3 v(z,t)}{\partial z\,\partial t^2} + 2\rho I\Omega \frac{\partial^2 u(z,t)}{\partial z\,\partial t} + EI \frac{\partial^3 v(z,t)}{\partial z^3}, \tag{2b}$$

$$M_x(z,t) = EI \frac{\partial^2 v(z,t)}{\partial z^2}, \qquad M_y(z,t) = -EI \frac{\partial^2 u(z,t)}{\partial z^2}. \tag{2c, d}$$

Laplace transform of equations (1) with zero initial conditions gives

$$EI \frac{\partial^4 \bar{u}(z,s)}{\partial z^4} - 2\rho I\Omega s \frac{\partial^2 \bar{v}(z,s)}{\partial z^2} - \rho I s^2 \frac{\partial^2 \bar{u}(z,s)}{\partial z^2} + \rho A s^2 \bar{u}(z,s) = \bar{f}_x(z,s), \tag{3a}$$

$$EI \frac{\partial^4 \bar{v}(z,s)}{\partial z^4} + 2\rho I\Omega s \frac{\partial^2 \bar{u}(z,s)}{\partial z^2} - \rho I s^2 \frac{\partial^2 \bar{v}(z,s)}{\partial z^2} + \rho A s^2 \bar{v}(z,s) = \bar{f}_y(z,s), \tag{3b}$$

where the over-bar denotes Laplace transformation with respect to time, and s is the complex Laplace transform parameter. Equations (3) are cast into the spatial state–space form

$$\frac{\partial}{\partial z}\boldsymbol{\eta}(z,s) = F(s)\boldsymbol{\eta}(z,s) + \boldsymbol{\upsilon}(z,s), \qquad 0 \leqslant z \leqslant L, \tag{4}$$

where the state–space vector $\boldsymbol{\eta}(z,s)$ and the force vector $\boldsymbol{\upsilon}(z,s)$ are given by

$$\boldsymbol{\eta}(z,s) = \left\{\bar{u} \quad \frac{\partial \bar{u}}{\partial z} \quad \frac{\partial^2 \bar{u}}{\partial z^2} \quad \frac{\partial^3 \bar{u}}{\partial z^3} \quad \bar{v} \quad \frac{\partial \bar{v}}{\partial z} \quad \frac{\partial^2 \bar{v}}{\partial z^2} \quad \frac{\partial^3 \bar{v}}{\partial z^3}\right\}^T, \tag{5a}$$

$$\boldsymbol{\upsilon}(z,s) = \{0 \quad 0 \quad 0 \quad \bar{f}_x/EI \quad 0 \quad 0 \quad 0 \quad \bar{f}_y/EI\}^T, \tag{5b}$$

and $F(s)$ is an eight-by-eight state–space matrix consisting of the shaft parameters and s. Also, the boundary conditions can be written in the matrix form

$$M_b\,\boldsymbol{\eta}(0,s) + N_b\,\boldsymbol{\eta}(L,s) = \boldsymbol{\gamma}(s), \tag{6}$$

where $\boldsymbol{\gamma}(s)$ is the vector of boundary disturbances, and the entries of the matrices M_b and N_b can be easily changed to assign different boundary conditions. The solution to the state–space equation (4) with the boundary conditions (6) is [27]

$$\boldsymbol{\eta}(z,s) = \int_0^L G(z,\xi,s)\boldsymbol{\upsilon}(\xi,s)\,\mathrm{d}\xi + H(z,s)\boldsymbol{\gamma}(s), \tag{7}$$

where the distributed transfer functions $G(z,\xi,s)$ and $H(z,s)$ of the shaft component are in the exact and closed form

$$G(z,\xi,s) = \begin{cases} H(z,s)M_b\,\mathrm{e}^{-F(s)\xi}, & \xi \leqslant z, \\ -H(z,s)N_b\,\mathrm{e}^{F(s)(L-\xi)}, & \xi \geqslant z. \end{cases} \tag{8a}$$

$$H(z,s) = \mathrm{e}^{F(s)z}(M_b + N_b\,\mathrm{e}^{F(s)L})^{-1}. \tag{8b}$$

Define the displacement vector and internal force vector of the shaft by

$$\boldsymbol{\alpha}(z,s) = \{\bar{u}(z,s) \quad \bar{\theta}_x(z,s) \quad \bar{v}(z,s) \quad \bar{\theta}_y(z,s)\}^T, \tag{9a}$$

and

$$\boldsymbol{\sigma}(z,s) = \{\bar{F}_x(z,s) \quad \bar{M}_x(z,s) \quad \bar{F}_y(z,s) \quad \bar{M}_y(z,s)\}^T, \tag{9b}$$

where $\bar{\theta}_x(z, s) = -\partial\bar{v}/\partial z$ and $\bar{\theta}_y(z, s) = \partial\bar{u}/\partial z$ are the rotation angles of the shaft about the x- and y-axes, and the elements of $\boldsymbol{\sigma}(z, s)$ are the Laplace transforms of the internal forces in equations (2). It follows from equations (2) and (9) that

$$\boldsymbol{\alpha}(z, s) = E_\alpha\,\boldsymbol{\eta}(z, s), \qquad \boldsymbol{\sigma}(z, s) = E_\sigma(s)\boldsymbol{\eta}(z, s), \tag{10a, b}$$

where E_α is a 4×8 constant matrix whose elements are 0 and ± 1, and

$$E_\sigma(s) = \begin{bmatrix} 0 & -\rho I s^2 & 0 & EI & 0 & -2\rho I\Omega s & 0 & 0 \\ 0 & 0 & 0 & 0 & 0 & 0 & EI & 0 \\ 0 & 2\rho I\Omega s & 0 & 0 & 0 & -\rho I s^2 & 0 & EI \\ 0 & 0 & -EI & 0 & 0 & 0 & 0 & 0 \end{bmatrix}.$$

One key step in the distributed transfer function modelling is to express the response of the shaft by its displacements at nodes i and j. Define the nodal displacements vectors

$$\boldsymbol{\alpha}_i(s) = \boldsymbol{\alpha}(0, s), \qquad \boldsymbol{\alpha}_j(s) = \boldsymbol{\alpha}(L, s). \tag{11}$$

Treat the nodal displacements as boundary disturbances by setting

$$\boldsymbol{\gamma}(s) = \begin{pmatrix} \boldsymbol{\alpha}_i(s) \\ \boldsymbol{\alpha}_j(s) \end{pmatrix}, \tag{12}$$

and form appropriate boundary matrices M_b and N_b in equation (6). By equations (7), (10) and (12), the displacements and internal forces of the shaft are expressed by

$$\begin{pmatrix} \boldsymbol{\alpha}(z, s) \\ \boldsymbol{\sigma}(z, s) \end{pmatrix} = \begin{bmatrix} E_\alpha \\ E_\sigma(s) \end{bmatrix} \int_0^L G(z, \xi, s)\boldsymbol{\upsilon}(\xi, s)\,\mathrm{d}\xi + \begin{bmatrix} E_\alpha \\ E_\sigma(s) \end{bmatrix} H(z, s) \begin{pmatrix} \boldsymbol{\alpha}_i(s) \\ \boldsymbol{\alpha}_j(s) \end{pmatrix}. \tag{13}$$

Hence, the displacements and internal forces at every point of the shaft are completely determined once the nodal displacements are known.

The above modelling technique is not limited to Euler–Bernoulli beams. Rayleigh and Timoshenko beam models counting on rotary inertia and shear deformation can also be easily cast into the same state–space form, equation (4), and this is done by simply changing the entries of the matrices $F(s)$, M_b and N_b. Also, torsional and longitudinal deformations, internal/material damping, distributed constraints (e.g., elastic foundation) can be modelled without any complication in analysis. Indeed, for different rotating shaft models under arbitrary loads and boundary conditions, the distributed transfer function modelling has the same formula, equation (7), and does not require specific derivations.

2.2. NON-UNIFORM FLEXIBLE ROTATING SHAFT

If the geometric and material parameters of a flexible shaft are dependent upon the spatial co-ordinate z, the state–space matrix in equation (4) becomes a function of z, namely, $F = F(z, s)$. In this case, the distributed transfer function solution, equation (7), is still valid if the exponential matrix $e^{F(s)z}$ in equation (8) is replaced by the fundamental matrix $\boldsymbol{\Phi}(z, s)$, which is the solution of

$$\frac{\partial}{\partial z}\boldsymbol{\Phi}(z, s) = F(z, s)\boldsymbol{\Phi}(z, s), \qquad \boldsymbol{\Phi}(0, s) = I. \tag{14}$$

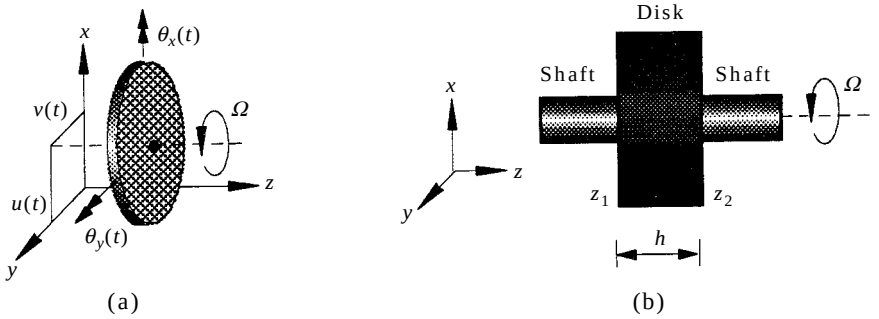

Figure 3. Rigid rotating disks: (a) thin and (b) thick disk.

One accurate and efficient way to determine $\mathbf{\Phi}(z, s)$ is the step function approximation given in reference [28]. The non-uniform shaft is approximated by n_s serially connected uniform shaft segments $\Delta_k = (z_{k-1}, z_k)$, $k = 1, 2, \ldots, n_s$, where the nodes z_k are such that $0 = z_0 < z_1 < \cdots < z_{n_s} = L$. Within the kth segment, the fundamental matrix is of the form

$$\mathbf{\Phi}(z, s) = \mathrm{e}^{F_k(s)(z - z_{k-1})} D_k, \qquad z \in \Delta_k, \tag{15}$$

where $F_k(s) = F(z_{k-1}/2 + z_k/2, s)$, and D_k is a constant matrix to be determined. At node z_k, where the segments Δ_k and Δ_{k+1} are inter-connected, force balance and displacement continuity leads to

$$\mathbf{\Phi}(z_k + 0, s) = T_k(s)\mathbf{\Phi}(z_k - 0, s), \tag{16}$$

where $T_k(s)$ is a constant matrix consisting of the geometric and material coefficients of the shaft. Through connection of all the segments, the matrices D_k are obtained as

$$D_1 = I; \qquad D_k = \prod_{j=1}^{k-1} T_j(s)\, \mathrm{e}^{F_j(s)(z_j - z_{j-1})}, \qquad k = 2, \ldots, n_s. \tag{17}$$

Thus, by equations (15) and (17), $\mathbf{\Phi}(z, s)$ at any z is completely determined. The response of the non-uniform shaft can then be estimated by equations (7) and (8), with $\mathrm{e}^{F(s)z}$ replaced by $\mathbf{\Phi}(z, s)$. Moreover, a response-nodal displacement relation similar to equation (13) can be established.

The above modelling is exact if the physical system in consideration is a stepped flexible shaft.

2.3. RIGID ROTATING DISKS

In Figure 3(a) a rotating rigid disk of negligible thickness is subject to external forces F_x and F_y at its center and external force moments M_x and M_y (not shown in the figure). The displacements u and v at the disk center and the disk rotations θ_x and θ_y are governed by

$$F_x(t) = m_D\, \ddot{u}(t), \qquad F_y(t) = m_D\, \ddot{v}(t), \tag{18a, b}$$

and

$$M_x(t) = I_{Dx}\, \ddot{\theta}_x(t) + I_{Dz}\, \Omega \dot{\theta}_y(t), \qquad M_y(t) = I_{Dx}\, \ddot{\theta}_y - I_{Dz}\, \Omega \dot{\theta}_x(t), \tag{18c, d}$$

where m_D is the disk mass, and I_{Dx} and I_{Dz} are the mass moments of the disk about the x- and z-axes. Laplace transform of equation (18) leads to the force-displacement relation for the disk,

$$\begin{bmatrix} \bar{F}_x \\ \bar{M}_x \\ \bar{F}_y \\ \bar{M}_y \end{bmatrix} = \begin{bmatrix} M_D s^2 & 0 & 0 & 0 \\ 0 & I_{Dx} s^2 & 0 & I_{Dz} \Omega s \\ 0 & 0 & M_D s^2 & 0 \\ 0 & -I_{Dz} \Omega s & 0 & I_{Dx} s^2 \end{bmatrix} \begin{bmatrix} \bar{u} \\ \bar{\theta}_x \\ \bar{v} \\ \bar{\theta}_y \end{bmatrix} = K_d(s) \begin{bmatrix} \bar{u} \\ \bar{\theta}_x \\ \bar{v} \\ \bar{\theta}_y \end{bmatrix}. \tag{19}$$

In Figure 3(b) a rotating rigid disk of thickness h is connected to two flexible shaft segments at two sides $z = z_1$ and z_2. The thick disk can also be used as a model for rigid rotors. In the Laplace transform domain, let the displacements and internal forces of the shafts at the disk-connecting points be $\bar{u}(z_i, s)$, $\bar{v}(z_i, s)$, $\bar{\theta}_x(z_i, s)$ and $\bar{\theta}_y(z_i, s)$, and $\bar{F}_x(z_i, s)$, $\bar{F}_y(z_i, s)$, $\bar{M}_x(z_i, s)$ and $M_y(z_i, s)$, $i = 1, 2$. Force balance of the disk yields

$$\bar{F}_x(z_1, s) + \bar{F}_x(z_2, s) = m_D \left(s^2 \bar{u}(z_1, s) + \frac{h}{2} s^2 \bar{\theta}_y(z_1, s) \right), \tag{20a}$$

$$\bar{F}_y(z_1, s) + \bar{F}_y(z_2, s) = m_D \left(s^2 \bar{v}(z_1, s) - \frac{h}{2} s^2 \bar{\theta}_x(z_1, s) \right), \tag{20b}$$

$$\bar{M}_x(z_1, s) + \bar{M}_x(z_2, s) + \frac{h}{2} \bar{F}_y(z_1, s) - \frac{h}{2} \bar{F}_y(z_2, s) = I_{Dx} s^2 \bar{\theta}_x(z_1, s) + I_{Dz} \Omega s \bar{\theta}_y(z_1, s), \tag{20c}$$

$$\bar{M}_y(z_1, s) + \bar{M}_y(z_2, s) - \frac{h}{2} \bar{F}_x(z_1, s) + \frac{h}{2} \bar{F}_x(z_2, s) = I_{Dx} s^2 \bar{\theta}_x(z_1, s) - I_{Dz} \Omega s \bar{\theta}_x(z_1, s), \tag{20d}$$

where the parameters m_D, I_{Dx} and I_{Dz} have the same meaning as those in equations (18). According to equations (2), the internal forces can be expressed in terms of the shaft displacements and their spatial derivatives. In other words, the displacements and internal forces at $z = z_2$ are related to those at $z = z_1$ by

$$\begin{bmatrix} \boldsymbol{\sigma}(z_1, s) \\ \boldsymbol{\sigma}(z_2, s) \end{bmatrix} = -K_d(s) \begin{bmatrix} \boldsymbol{\alpha}(z_1, s) \\ \boldsymbol{\alpha}(z_2, s) \end{bmatrix}, \tag{21}$$

where $\boldsymbol{\alpha}$ and $\boldsymbol{\sigma}$ have been defined in equations (6), and $K_d(s)$ is a matrix consisting of the coefficients in equations (2) and (20).

2.4. BEARINGS

Bearings and seals are commonly modelled by a set of linear springs and dampers, as shown in Figure 4(a) where k_{xx}, k_{xy}, k_{yx} and k_{yy} are spring coefficients and c_{xx}, c_{xy}, c_{yx} and c_{yy} are damping coefficients. For such a model, the s-domain constraint forces applied to the connecting shaft by the bearing are expressed by

$$\mathbf{f}_c(s) = -K_b(s) \boldsymbol{\alpha}(s), \tag{22}$$

where

$$\mathbf{f}_c(s) = \begin{Bmatrix} \bar{F}_x \\ \bar{M}_x \\ \bar{F}_y \\ \bar{M}_y \end{Bmatrix}, \quad \boldsymbol{\alpha}(s) = \begin{Bmatrix} \bar{u} \\ \bar{\theta}_x \\ \bar{v} \\ \bar{\theta}_y \end{Bmatrix}, \quad K_b(s) = \begin{bmatrix} k_{xx} + c_{xx} s & 0 & k_{xy} + c_{xy} s & 0 \\ 0 & 0 & 0 & 0 \\ k_{yx} + c_{yx} s & 0 & k_{yy} + c_{yy} s & 0 \\ 0 & 0 & 0 & 0 \end{bmatrix},$$

with $\bar{u}$, $\bar{v}$, $\bar{\theta}_x$ and $\bar{\theta}_y$ being the transverse displacements and rotations of the shaft at the bearing location. The modelling herein is also valid for fluid film bearings whose stiffness and damping coefficients are functions of the rotating speed Ω [5].

The bearing model shown in Figure 4(a) only describes the radial forces of the bearings. This is because the shaft model, equations (1), is a Euler–Bernoulli beam, i.e., infinite torsional stiffness has been assumed. The $K_b(s)$, however, can be modified to include couples or tangential forces of the bearings. In that case, torsional deformation of the flexible shaft should also be modelled, as discussed at the end of section 2.1.

In Figure 4(b), two co-axial rotors are linked by an inter-shaft bearing, where the inner and outer rotors may have different rotation speeds. Let $\boldsymbol{\alpha}_{inner}(s)$ and $\boldsymbol{\alpha}_{outer}(s)$ be the vectors of the displacements of the inner and outer shafts at the bearing–shaft connection locations. By the bearing model given in Figure 4(a), the vector of the constraints forces that are applied to the inner shaft by the bearing is of the form

$$\mathbf{f}_c(s) = -K_b(s)(\boldsymbol{\alpha}_{inner}(s) - \boldsymbol{\alpha}_{outer}(s)), \tag{23}$$

where $K_b(s)$ has been given in equation (22). The constraint forces applied to the outer shaft by the bearing are expressed by $-\mathbf{f}_c(s)$.

2.5. GEARS

Four flexible shaft segments (I, II, III and IV) are coupled by a pair of gears; see Figure 5(a) where 1, 2, . . . , 6 are node numbers, and $\boldsymbol{\alpha}_j(s)$ is the nodal displacement vector at node j. A free-body diagram of the gears is shown in Figure 5(b), where $\boldsymbol{\sigma}_2^-(s)$ and $\boldsymbol{\sigma}_2^+(s)$ represent the internal forces applied to the upper gear by segments I and II, respectively, $\boldsymbol{\sigma}_5^-(s)$ and $\boldsymbol{\sigma}_5^+(s)$ the internal forces applied to the lower gear by segments III and IV, and $\mathbf{q}_c(s)$ describes the action and reaction forces between the two gears. The $\boldsymbol{\alpha}_j(s)$, $\boldsymbol{\sigma}_2^{\pm}(s)$ and $\boldsymbol{\sigma}_5^{\pm}(s)$ are estimated by equation (13).

Physically, the gear coupling also causes action and reaction couples in the axial direction. The couples are ignored in $\mathbf{q}_c(s)$ because of the Euler–Bernoulli beam model of the shaft segments. Like in the bearing modelling (section 2.4), those couples can be easily modelled through consideration of the torsional deformation of the shaft segments.

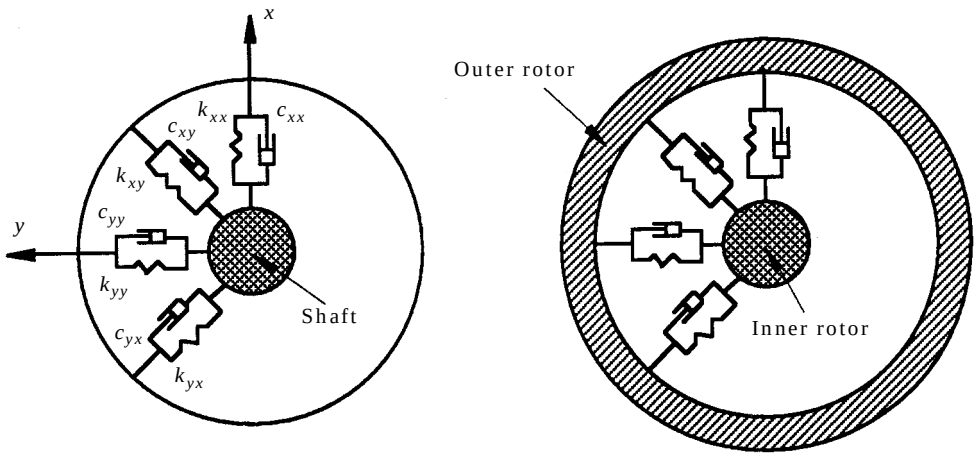

(a) (b)

Figure 4. Bearings: (a) a spring-damper model and (b) an inter-shaft bearing linking two co-axial rotors.

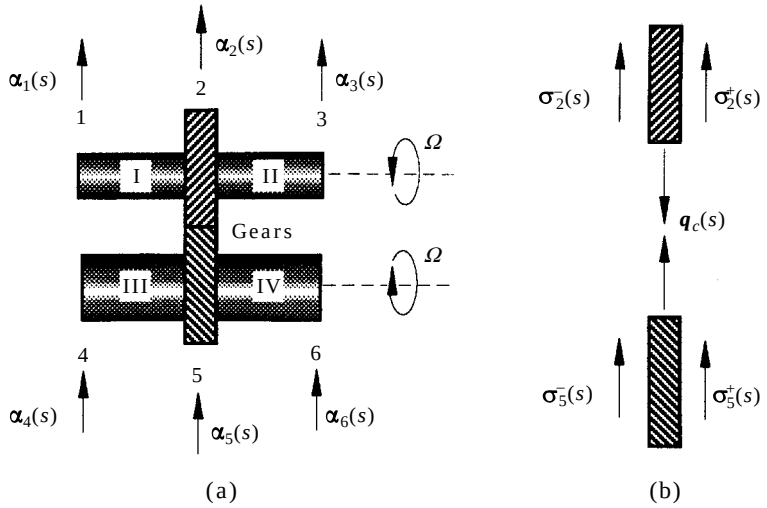

Figure 5. Coupling of flexible shafts by gears: (a) side view and (b) gear interaction.

Force balance on the gears yields

$$M_{g2}(s)\boldsymbol{\alpha}_2(s) = \boldsymbol{\sigma}_2^-(s) + \boldsymbol{\sigma}_2^+(s) - \mathbf{q}_c(s), \qquad M_{g5}(s)\boldsymbol{\alpha}_5(s) = \boldsymbol{\sigma}_5^-(s) + \boldsymbol{\sigma}_5^+(s) + \mathbf{q}_c(s), \quad (24a, b)$$

where the matrices $M_{g2}(s)$ and $M_{g5}(s)$ characterize the inertial and gyroscopic effects of the upper and lower gears, respectively. For the gears being perfectly coupled, their kinematic relation is

$$\boldsymbol{\alpha}_5(s) = C_g\,\boldsymbol{\alpha}_2(s), \quad (25)$$

where C_g is a non-singular constant matrix. Elimination of $\boldsymbol{\alpha}_5(s)$ from equations (24) and (25) gives

$$(M_{g2}(s) + M_{g5}(s)C_g)\boldsymbol{\alpha}_2(s) = \boldsymbol{\sigma}_2^-(s) + \boldsymbol{\sigma}_2^+(s) + \boldsymbol{\sigma}_5^-(s) + \boldsymbol{\sigma}_5^+(s). \quad (26)$$

According to equation (13), $\boldsymbol{\sigma}_2^-(s)$ can be expressed by the displacements of segment I at nodes 1 and 2. Likewise, $\boldsymbol{\sigma}_2^+(s)$, $\boldsymbol{\sigma}_5^-(s)$ and $\boldsymbol{\sigma}_5^+(s)$ are expressible by the nodal displacements of segments II, III and IV. Hence, substituting equation (13) into equation (26) leads to

$$\sum_{i=1}^{6} K_{2i}(s)\boldsymbol{\alpha}_i(s) = \mathbf{f}_{T2}(s), \quad (27)$$

where $\mathbf{f}_{T2}(s)$ is the vector of transmitted forces at node 2, and the stiffness matrices $K_{2i}(s)$ are composed of the elements of $M_{g2}(s) + M_{g5}(s)C_g$ and distributed transfer functions of the shaft segments. It is seen that the gears couple the displacements at all the six nodes.

3. DISTRIBUTED TRANSFER FUNCTION SYNTHESIS

In the previous section, the transfer functions of distributed and lumped components have been derived. In this section, the complex system is assembled from its components by the use of these transfer functions.

Assume that the complex rotor system is decomposed into a number of distributed and lumped components that are inter-connected at n nodes. At node j, flexible shaft components A (bounded by nodes i and j) and B (bounded by nodes j and l) are inter-connected; see Figure 6. Also, at the node may be a bearing and a thin rigid disk

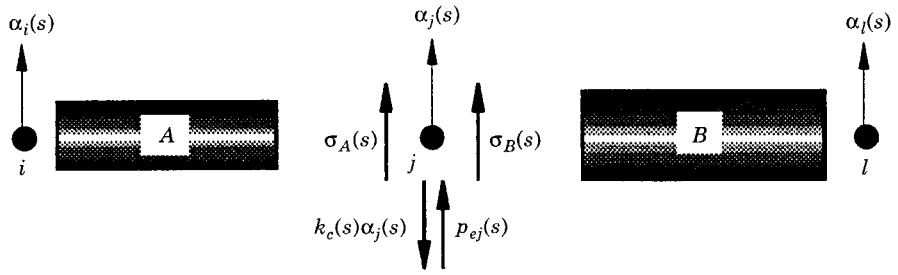

Figure 6. Assembly of components at node j.

(not shown in the figure). The resultant constraint forces of the bearing and disk are expressed by $-K_c(s)\boldsymbol{\alpha}_j(s)$, where $\boldsymbol{\alpha}_j(s)$ is the nodal displacement vector of node j, and the constraint matrix $K_c(s)$ can be obtained from equations (19) and (22). Let $\boldsymbol{\sigma}_A(s)$ and $\boldsymbol{\sigma}_B(s)$ be the vectors of the internal forces applied at node j by components A and B, respectively, and $\mathbf{p}_{ej}(s)$ the vector of the pointwise external forces at node j. Force balance at the node gives

$$\boldsymbol{\sigma}_A(s) + \boldsymbol{\sigma}_B(s) - K_c(s)\boldsymbol{\alpha}_j(s) + \mathbf{p}_{ej}(s) = 0. \tag{28}$$

According to equation (13), the internal forces are of the form

$$\boldsymbol{\sigma}_A(s) = -K_i^{(A)}(s)\boldsymbol{\alpha}_i(s) - K_j^{(A)}(s)\boldsymbol{\alpha}_j(s) + \mathbf{f}_{Tj}^{(A)}, \tag{29a}$$

$$\boldsymbol{\sigma}_B(s) = -K_j^{(B)}(s)\boldsymbol{\alpha}_j(s) - K_l^{(B)}(s)\boldsymbol{\alpha}_l(s) + \mathbf{f}_{Tj}^{(B)}, \tag{29b}$$

where the transmitted nodal force vectors $\mathbf{f}_{Tj}^{(A)}$ and $\mathbf{f}_{Tj}^{(B)}$ are derivable from the first term of equation (13), and the matrices like $K_i^{(A)}$ from the second term. Substituting equations (29) into equation (28) yields the dynamic equilibrium equation about node j:

$$K_i^{(A)}(s)\boldsymbol{\alpha}_i(s) + (K_j^{(A)}(s) + K_j^{(B)}(s) + K_c(s))\boldsymbol{\alpha}_j(s) + K_l^{(B)}(s)\boldsymbol{\alpha}_l(s) = \mathbf{f}_{Tj}^{(A)} + \mathbf{f}_{Tj}^{(B)} + \mathbf{p}_{ej}(s). \tag{30}$$

If component B is a thick disk, a force-displacement relation similar to equation (29b) can be derived from equation (21). If at node j an inner rotor is connected to a co-axial outer rotor by an inter-shaft bearing (Figure 4(b)), the constraint force vector $-K_c(s)\boldsymbol{\alpha}_j(s)$ in equation (28) is replaced by $\mathbf{f}_c(s)$ in equation (23), in which $\boldsymbol{\alpha}_{inner}(s) = \boldsymbol{\alpha}_j(s)$, and as such, the force balance at the node will involve an additional nodal displacement vector, $\boldsymbol{\alpha}_{outer}(s)$. If a gear is located at node j, then by equation (27), force balance at the node will involve the nodal displacements at six nodes. In any of the above cases, the dynamic equilibrium equation at node j can be written as

$$K_{ji}(s)\boldsymbol{\alpha}_i(s) + K_{jj}(s)\boldsymbol{\alpha}_j(s) + K_{jl}(s)\boldsymbol{\alpha}_l(s) + \cdots + K_{jm}(s)\boldsymbol{\alpha}_m(s) = \mathbf{q}_j(s), \tag{31}$$

where $\boldsymbol{\alpha}_i(s)$, $\boldsymbol{\alpha}_j(s)$, $\boldsymbol{\alpha}_l(s)$, . . . , $\boldsymbol{\alpha}_m(s)$ are all the nodal displacements that are involved in the force balance at node j, $K_{ji}(s)$ etc. are stiffness matrices derivable from equations like equation (30), and $\mathbf{q}_j(s)$ is the resultant of the transmitted nodal forces and pointwise external forces.

Force balance at all the n nodes and assembly of the resulting equations yields a global dynamic equilibrium equation,

$$K(s)\mathbf{U}(s) = \mathbf{Q}(s), \tag{32}$$

where $K(s)$ is the global dynamic stiffness matrix of the complex system composed of $K_{ji}(s)$, $j, i = 1, 2, \ldots, n$, $\mathbf{U}(s) = \{\boldsymbol{\alpha}_1^T(s) \cdots \boldsymbol{\alpha}_n^T(s)\}^T$ is the unknown global nodal displacement vector, and $\mathbf{Q}(s) = \{\mathbf{q}_1^T(s) \cdots \mathbf{q}_n^T(s)\}^T$ is the global nodal force vector. In the above synthesis, no approximation or discretization has been made. Note that the boundary conditions of the complex rotor system have been automatically imposed at the component level; see equations (6) and (7). Thus, upon its formation, equation (32) is ready to be solved.

4. DYNAMIC ANALYSIS

With the distributed transfer function formulation, the solutions to various dynamic problems of complex flexible rotor systems can be obtained in exact and closed form.

4.1. EIGENSOLUTIONS

The eigenvalue problem of the complex rotor system, by equation (32), is

$$K(s)\mathbf{U}(s) = 0. \tag{33}$$

The eigenvalues λ_i of the complex system are the roots of the characteristic equation

$$\det K(\lambda_i) = 0, \qquad i = 1, 2, \ldots . \tag{34}$$

The eigenfunction or mode shape corresponding to the ith eigenvalue λ_i is obtained by substituting the nontrivial solution $\mathbf{U}$ of the equation $K(\lambda_k)\mathbf{U} = 0$ into equation (13). Note that equation (13) also gives the modal stresses.

4.2. DYNAMIC RESPONSE DUE TO UNBALANCED MASS

A flexible rotor system has an unbalanced mass m_u of eccentricity e at a node. The shaft rotation induces a centrifugal force at the node whose x- and y-projections are

$$p_x = m_u e\, \Omega^2 \cos \Omega t, \qquad p_y = m_u e\, \Omega^2 \sin \Omega t. \tag{35}$$

Assume that there are no external loads. Then, the Laplace transforms of p_x and p_y are the only two non-zero entries of the nodal force vector $\mathbf{Q}(s)$ in equation (32). Write

$$\begin{pmatrix} p_x \\ p_y \end{pmatrix} = \mathrm{Im}\,(\chi_0\, \mathrm{e}^{J\Omega t}), \qquad \chi_0 = m_u e\, \Omega^2 \begin{pmatrix} J \\ 1 \end{pmatrix}, \tag{36}$$

where $J = \sqrt{-1}$. Since, p_x and p_y are harmonic excitations, by equation (32), the vector $\mathbf{U}(t)$ of the steady state displacements at all the nodes are of the form

$$\mathbf{U}(t) = \mathrm{Im}\,(\Xi(J\Omega)\chi_0\, \mathrm{e}^{J\Omega t}), \tag{37}$$

where $\Xi(J\Omega)$ is obtained from proper partition of the inversed matrix $K^{-1}(J\Omega)$, corresponding to the positions of $\bar{p}_x$ and $\bar{p}_y$ in $\mathbf{Q}(s)$. The steady state response of a flexible shaft component is obtained by substituting equation (37) into equation (13):

$$\boldsymbol{\alpha}(z, t) = \mathrm{Im}\,(A(z, \Omega)\, \mathrm{e}^{J\Omega t}) = A_I(z, \Omega) \cos \Omega t + A_R(z, \Omega) \sin \Omega t, \tag{38}$$

where $\boldsymbol{\alpha}(z, t)$ is the time-domain displacement vector of the shaft component, the complex matrix

$$A(z, \Omega) = E_\alpha H(z, J\Omega)\pi(J\Omega)\chi_0, \tag{39}$$

A_R and A_I are the real and imaginary parts of $A(z, \Omega)$, respectively, and the matrix $\pi(J\Omega)$ is composed of those columns of $\Xi(J\Omega)$ which are related to the nodal displacements of the shaft component. The internal forces of the shaft component can be similarly determined.

4.3. WHIRLING MOTION OF UNBALANCED ROTORS

Consider the unbalanced flexible rotor analyzed in section 4.2. At point z (either a node or an interior point of a flexible shaft component), the whirling motion (the transverse displacements of the rotor geometric center) is described by

$$\begin{pmatrix} u(t) \\ v(t) \end{pmatrix} = \begin{bmatrix} A_1 & B_1 \\ A_2 & B_2 \end{bmatrix} \begin{pmatrix} \cos \Omega t \\ \sin \Omega t \end{pmatrix}, \tag{40}$$

where A_i and B_i are the elements of the matrices A_I and A_R in equation (38). The whirling is forward (backward) if the scalar triple product $\Omega \mathbf{e}_3 . (\mathbf{r}(t) \times \mathrm{d}\mathbf{r}(t)/\mathrm{d}t)$ is positive (negative), where $\mathbf{r}(t) = u(t)\mathbf{e}_1 + v(t)\mathbf{e}_2$ is the displacement vector of the shaft geometric center, and $\mathbf{e}_1$, $\mathbf{e}_2$ and $\mathbf{e}_3$ are the unit vectors of the fixed co-ordinate system $oxyz$. It follows that the whirling motion is forward (backward) whirl if $A_1 B_2 - A_2 B_1$ is positive (negative). This result is in agreement with what is given in reference [12] although the current study adopts an exact and closed-form PDE model of the complex flexible rotor system for the first time. Define a whirl direction indicator

$$\Psi = \begin{cases} \operatorname{sgn}(A_1 B_2 - A_2 B_1), & \text{for } A_1 B_2 - A_2 B_1 \neq 0, \\ 0, & \text{for } A_1 B_2 - A_2 B_1 = 0. \end{cases} \tag{41}$$

The whirl direction of the rotor is therefore detected as follows:

$$\text{forward whirl condition:} \qquad \Psi = 1, \tag{42a}$$

$$\text{backward whirl condition:} \qquad \Psi = -1. \tag{42b}$$

When $\Psi \neq 0$, the whirl orbit by equation (40) is an ellipse

$$ax^2 + 2bxy + cy^2 = 1, \tag{43}$$

where the coefficients a, b and c are determined by

$$\begin{bmatrix} a & b \\ b & c \end{bmatrix} = \begin{bmatrix} A_1 & B_1 \\ A_2 & B_2 \end{bmatrix}^T \begin{bmatrix} A_1 & B_1 \\ A_2 & B_2 \end{bmatrix}^{-1} = \frac{1}{(A_1 B_2 - A_2 B_1)^2} \begin{bmatrix} A_2^2 + B_2^2 & -A_1 A_2 - B_1 B_2 \\ -A_1 A_2 - B_1 B_2 & A_1^2 + B_1^2 \end{bmatrix}.$$

When $\Psi = 0$, the trajectory of the rotor at point z becomes a straight line,

$$A_2 x - A_1 y = 0, \qquad \text{for } |x| \leqslant \sqrt{A_1^2 + B_1^2}. \tag{44}$$

The results obtained in this section differ from the previous ones in that without discretization and approximation, the whirl direction and trajectory for a complex rotor system of multiple flexible and rigid components at any location are precisely predicted.

4.4. CRITICAL SPEEDS

The critical speed of a rotor system is a specific rotation speed of the rotor at which the amplitude of the system dynamic response peaks, or becomes substantially large. In the following, two types of rotor systems are examined.

4.4.1. *Undamped rotor systems*

The characteristic equation of a complex flexible rotor system, by equation (33), is

$$\det K(s; \Omega) = 0, \tag{45}$$

where Ω is a rotation speed parameter indicating that the eigenvalues of a rotor system are dependent on its rotation speed. Because the rotor system is undamped, its critical speeds coincide with its natural frequencies [4]. So, the critical speeds are the roots of the equation

$$\det K(\pm J\Omega; \Omega) = 0, \qquad J = \sqrt{-1}, \tag{46}$$

which is obtained by substituting $s = \pm J\Omega$ in equation (45). The root $+J\Omega$ ($-J\Omega$) relates to forward (backward) critical speed.

4.4.2. *Unbalanced rotor systems*

The critical speeds of an unbalanced rotor system are determined based on its steady-state response, equation (40). In this case, the rotor system can have arbitrary damping. When $\Psi \neq 0$, the geometric center of the rotor system (point z) moves along the elliptic whirl orbit described by equation (43); the whirl direction is determined by the conditions (42). The long axis, A_m, of the ellipse represents the largest rotor displacement at point z, which, through co-ordinate rotation, is given by

$$A_m = \max\{\Delta(\theta_0), \Delta(\theta_0 + \pi/2)\}, \tag{47a}$$

where

$$\Delta(\theta) = \{a \cos^2\theta + 2b \sin\theta \cos\theta + c \sin^2\theta\}^{-1/2}, \qquad \theta_0 = \tfrac{1}{2}\arctan(2b/(a-c)),$$

and the coefficients, a, b and c are given in equation (43). When $\Psi = 0$, the trajectory of the rotor geometric center is a straight line. In this case, the largest displacement, by equation (44), is

$$A_m = \sqrt{A_1^2 + B_1^2 + A_2^2 + B_2^2}. \tag{47b}$$

The critical speeds of the rotor system are the local maximum points of the $A_m - \Omega$ curve.

4.5. EXTERNAL HARMONIC EXCITATIONS

A pointwise external harmonic force of the form

$$\begin{pmatrix} p_x \\ p_y \end{pmatrix} = \mathrm{Im}\,(\chi_0\, e^{J\omega t}), \qquad \chi_0 = \begin{pmatrix} \beta_x(\omega) \\ \beta_y(\omega) \end{pmatrix}, \tag{48}$$

is applied at a node, where ω is the excitation frequency, and $\beta_x(\omega)$ and $\beta_y(\omega)$ are complex and frequency-dependent amplitudes. Note that equation (36) is a special case of equation (48) if ω is replaced by Ω. Following the steps in section 4.2, the steady state response of the rotor system at any point is obtained as

$$\begin{pmatrix} u(t) \\ v(t) \end{pmatrix} = \begin{bmatrix} A_1 & B_1 \\ A_2 & B_2 \end{bmatrix} \begin{pmatrix} \cos\omega t \\ \sin\omega t \end{pmatrix}, \tag{49}$$

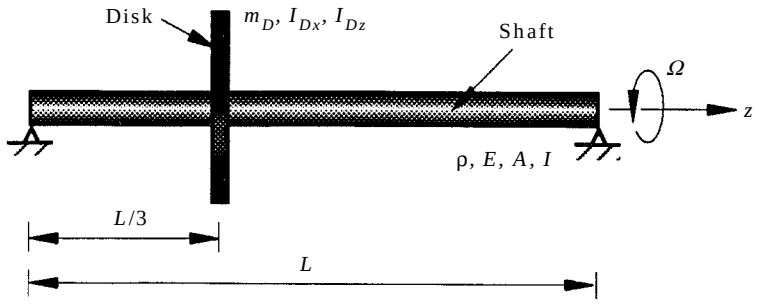

Figure 7. A uniform rotating shaft carrying a rigid thin disk.

where A_i and B_i are similar to those in equation (40) although the excitation frequency ω does not have to be the shaft rotation speed Ω. Following sections 4.3 and 4.4, similar results about the whirling motion and critical speeds can be obtained.

For spatially distributed harmonic excitations of frequency ω, the dynamic equilibrium equation (32) becomes $K(J\omega)\mathbf{U}(J\omega) = \mathbf{Q}(J\omega)$. Substituting the nodal displacement vector $\mathbf{U}(J\omega) = K^{-1}(J\omega)\mathbf{Q}(J\omega)$ into equation (13) yields an exact and closed-form prediction of the frequency response of the complex rotor system.

Besides the aforementioned dynamic problems, the distributed transfer function synthesis is also applicable to stability analysis and vibration control of complex flexible rotor systems [23]. The DTFS presented herein has two special features. First, without discretization, the method yields exact and closed-form solutions for various dynamic problems. Second, the method is convenient and efficient for systematic modelling and design of multi-body flexible rotor systems.

5. EXAMPLES

5.1. A UNIFORM FLEXIBLE SHAFT WITH A THIN DISK

A simply-supported, undamped, uniform flexible rotating shaft carries a rigid thin disk; see Figure 7. The parameters of the rotor system are: $L = 0{\cdot}4$ m, $\rho = 7800$ kg/m^3, $E = 2 \times 10^{11}$ N/m^2, $A = 3{\cdot}142 \times 10^{-4}$ m^2, $I = 7{\cdot}854 \times 10^{-9}$ m^4, $m_D = 16{\cdot}47$ kg, $I_{Dx} = 9{\cdot}427 \times 10^{-2}$ kg . m^2, $I_{Dz} = 0{\cdot}1861$ kg . m^2. The first and second forward critical speeds of the rotor are calculated by the DTFS using equation (46), and by an N-term Rayleigh–Ritz model using sine functions. The results are listed in Table 1. It is seen that as the number of terms N increases, the Rayleigh–Ritz prediction converges (from above) to that by the proposed DTFS.

TABLE 1

Critical speeds ($\Omega_{cr,k}$) of the uniform flexible shaft–disk system (rad/s)

		$\Omega_{cr,1}$	$\Omega_{cr,2}$
Rayleigh–Ritz method	$N = 2$	263·9	323·5
	4	263·4	307·9
	6	259·7	307·4
	8	258·2	307·1
	10	258·1	306·6
	12	257·0	306·5
	DTFS	254·1	306·1

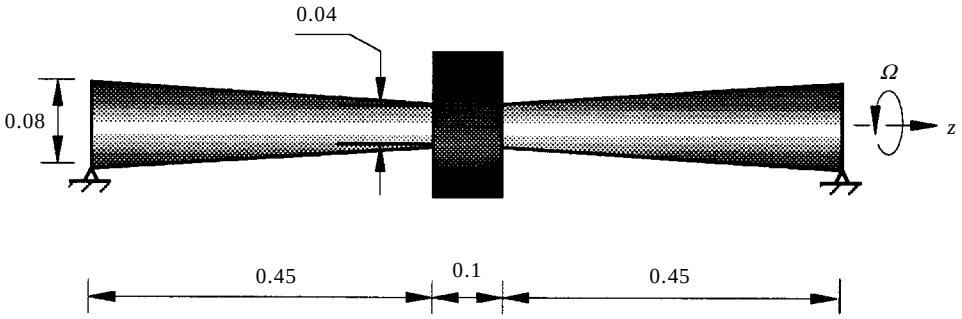

Figure 8. A non-uniform flexible shaft–disk system.

5.2. A NON-UNIFORM FLEXIBLE SHAFT WITH A THICK DISK

In Figure 8, a simply-supported rotor system is composed of two identical tapered flexible shafts of diameter $d = 2/25 - (4/45)z$, $0 \leqslant z \leqslant 0{\cdot}45$, and a rigid thick disk. The moment of inertia ($I = \pi d^4/64$) and cross-section area ($A = \pi d^2/4$) of the shafts are functions of z, rendering the shafts non-uniformly distributed. Other parameters of the rotor system are $\rho = 1$, $E = 100$, $m_D = 3{\cdot}1416 \times 10^{-3}$, $I_{Dx} = 1{\cdot}0472 \times 10^{-5}$, and $I_{Dz} = 1{\cdot}5701 \times 10^{-5}$. Here, all parameters are dimensionless. According to section 2.2, each flexible shaft is modelled as a sequence of serially connected stepped shaft segments. The first three critical speeds of the so-modelled rotor are listed in Table 2, where a fast convergence of the distributed transfer function prediction is seen. The critical speeds predicted by 2×9 shaft segments only deviate from those by 2×200 segments by less than 0·73, 0·33 and 0·74%, respectively.

5.3. A DUAL FLEXIBLE ROTOR SYSTEM

In Figure 9, two coaxial flexible rotors of different rotation speeds are linked by one inter-shaft bearing (Bearing 4). On each of the rotors are mountd two rigid thin disks. This kind of dual system is commonly seen in gas turbines and compressors [5]. In the literature, dual rotor systems have been studied by the finite element method [4]. In this example, the DTFS is applied to obtain exact solutions for the dual rotor system.

The rotor system is decomposed into seven flexible shaft segments by nine nodes $z_0, z_1, \ldots, z_8$; see Figure 9. The bearings are modelled in section 2.4, and the inter-shaft coupling is described in equation (23). The parameters of the rotor system are given in

TABLE 2

Critical speeds ($\Omega_{cr,k}$) of the non-uniform flexible shaft–disk system (n_s—number of shaft segments)

n_s	$\Omega_{cr,1}$	$\Omega_{cr,2}$	$\Omega_{cr,3}$
2×9	0·6521	6·0548	10·4289
2×18	0·6486	6·0696	10·3721
2×27	0·6479	6·0723	10·3612
2×45	0·6476	6·0736	10·3556
2×100	0·6474	6·0743	10·3531
2×150	0·6474	6·0744	10·3527
2×200	0·6474	6·0744	10·3526
2×250	0·6474	6·0744	10·3526

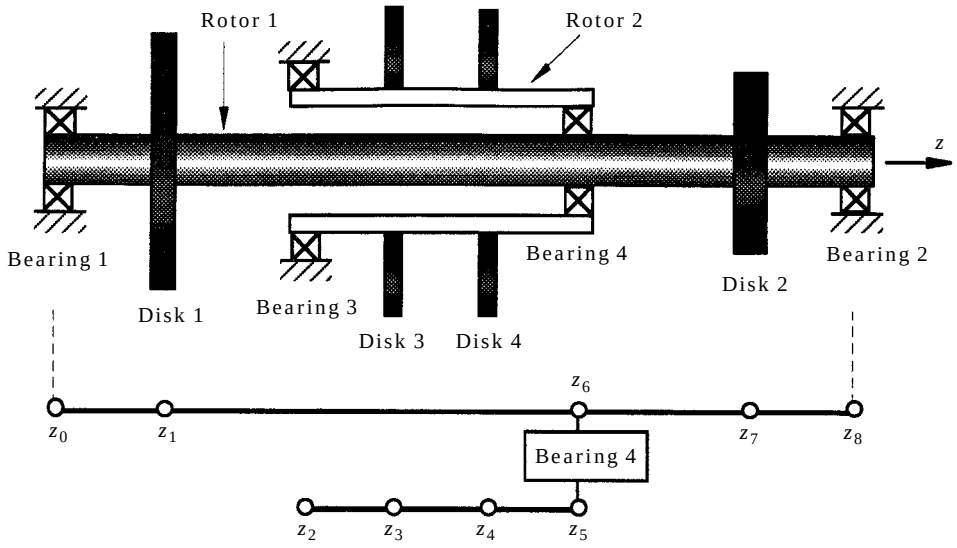

Figure 9. A dual flexible rotor system.

Table 3. The first eight eigenvalues of the dual rotor system, calculated by the DTFS, are given in Table 4. All the modes are stable (Re $\lambda_k < 0$).

To investigate unbalanced response, assume that an unbalanced mass $m_u e = 1{\cdot}0$ kg . m is at the location of Disk 2, node z_7. Let the rotation speeds of Rotors 1 and 2 be $\Omega_1 = \Omega$ and $\Omega_2 = 1{\cdot}5\Omega$, respectively. Figure 10 depicts the displacement amplitude A_m defined in equation (47a) versus the rotation speed parameter Ω, at the locations of Disks 2 and 4, respectively. From the $A_m - \Omega$ curves, the first two critical speeds of the rotor system are identified as $\Omega_{cr,1} = 765$, and $\Omega_{cr,2} = 1244$. The numerical simulation reveals that the whirl direction indicator $\Psi \equiv 1$ for any $\Omega > 0$. By equation (42a), only forward whirl is excited by the unbalanced mass.

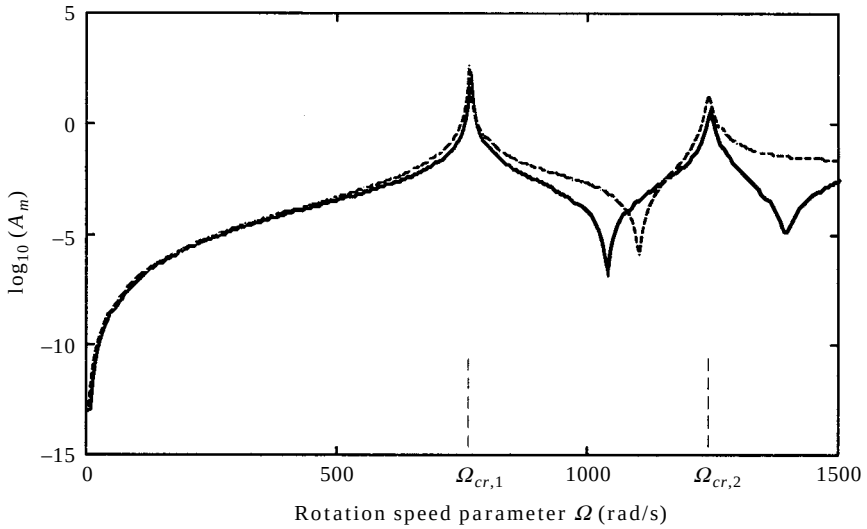

Figure 10. Amplitude of frequency response of the dual rotor system: ——, at Disk 2; - - - -, at Disk 4.

TABLE 3

Parameters of the dual flexible rotor system

Node locations (m)							
z_0	z_1	z_2	z_3	z_4	z_5/z_6	z_7	z_8
0·000	0·0762	0·1524	0·2032	0·3556	0·4064	0·4572	0·5080

Flexible rotors					
	Ω (r.p.m.)	ρ (kg/m^3)	E (N/m^2)	A (m^2)	I (m^4)
Rotor 1	10,000	7800	2×10^{11}	$7{\cdot}2975 \times 10^{-4}$	$4{\cdot}2373 \times 10^{-8}$
Rotor 2	15,000	7800	2×10^{11}	$8{\cdot}9192 \times 10^{-4}$	$3{\cdot}5101 \times 10^{-7}$

Bearings ($k_{xy} = k_{yx} = 0$ and $c_{xy} = c_{yx} = 0$ for all bearings)				
	k_{xx} (N/m) $\times 10^7$	k_{yy} (N/m) $\times 10^7$	c_{xx} (N/m/s) $\times 10^2$	c_{yy} (N/m/s) $\times 10^2$
Bearing 1	2·63	2·63	2·63	2·63
Bearing 2	1·75	1·75	1·75	1·75
Bearing 3	1·75	1·75	1·75	1·75
Bearing 4	0·875	0·875	0·875	0·875

Rigid disks			
	m_D (kg)	I_{Dx} (kg . m^2) $\times 10^{-2}$	I_{Dz} (kg . m^2) $\times 10^{-2}$
Disk 1	10·51	4·295	8·590
Disk 2	7·01	3·390	6·780
Disk 3	7·01	2·145	4·290
Disk 4	3·50	1·355	2·710

Backward whirl of the dual rotor system can be excited if the excitation is not "purely forward". To see this, consider a pointwise external harmonic force of the form

$$p_x = \omega^2 \cos \omega t, \qquad p_y = 0, \tag{50}$$

which is applied to node z_7. Let the excitation frequency coincide with the rotation speed of Rotor 1; i.e., $\omega = \Omega_1 = \Omega$. Assume that the rotor system has no unbalanced mass ($m_u e = 0$), and that the rotation speed of Rotor 2 is $\Omega_2 = 1{\cdot}5\Omega$. Plotted in Figure 11 are the amplitude A_m of the system frequency response and whirl direction indicator Ψ, at node z_7. It is seen that both forward and backward whirls exist. From the $A_m - \Omega$ curve, the

TABLE 4

Eigenvalues λ_k of the dual rotor system ($J = \sqrt{-1}$)

k	λ_k
1	$-4{\cdot}1750 \times 10^{-4} + J3{\cdot}3546 \times 10^2$
2	$-1{\cdot}3513 \times 10^{-2} + J8{\cdot}2532 \times 10^2$
3	$-2{\cdot}6300 \times 10^{-2} + J1{\cdot}0193 \times 10^3$
4	$-4{\cdot}5998 \times 10^{-2} + J1{\cdot}2367 \times 10^3$
5	$-6{\cdot}7111 \times 10^{-2} + J1{\cdot}4505 \times 10^3$
6	$-1{\cdot}3393 \times 10^{-1} + J1{\cdot}5798 \times 10^3$
7	$-1{\cdot}0851 \times 10^{-1} + J1{\cdot}6955 \times 10^3$
8	$-1{\cdot}3709 \times 10^{-1} + J1{\cdot}8010 \times 10^3$

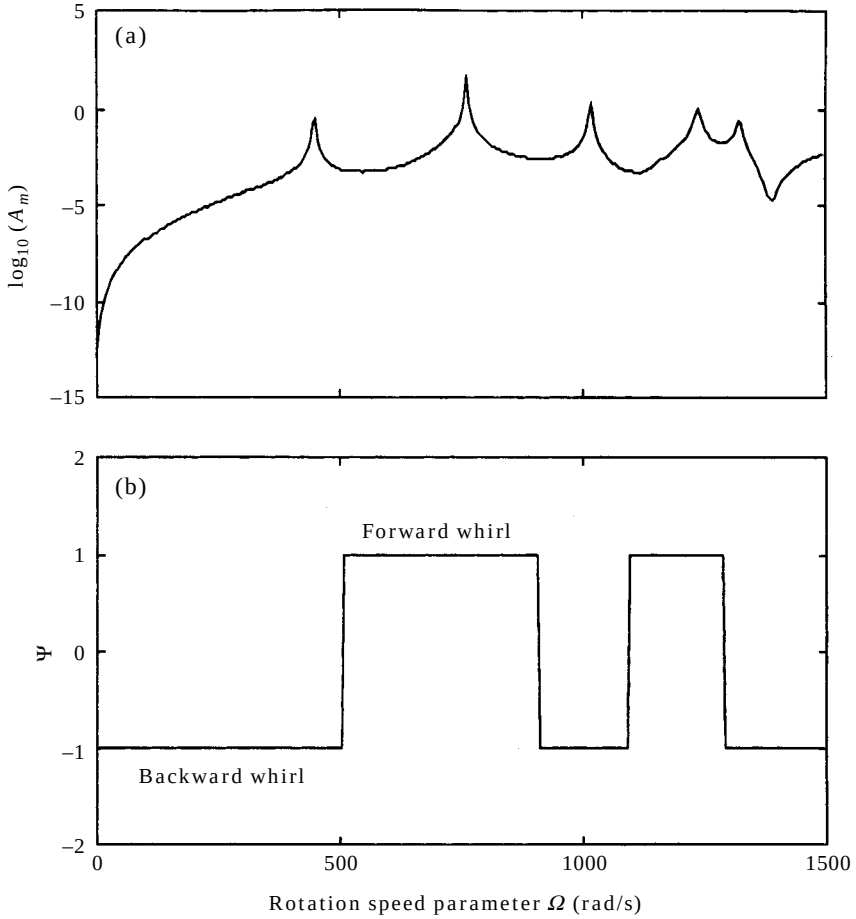

Figure 11. (a) The frequency response amplitude and (b) whirl direction indicator of the dual rotor system, at node z_7.

first five critical speeds of the rotor systems are determined as 453, 765, 1024, 1244 and 1332. The Ψ plot shows that the first, third and fifth critical speeds are backward speeds, and the second and fourth forward ones. Thus, the backward and forward critical speeds are in the interlacing relation, $\Omega^b_{cr,k} < \Omega^f_{cf,k} < \Omega^b_{cr,k+1}$, where the superscripts b and f denote backward and forward whirls, respectively.

If the rotor system is asymmetric, backward whirl can be excited by an unbalanced mass. To show this, change k_{yy} and c_{yy} of Bearing 2 in Table 3 to $k_{yy} = 2{\cdot}65 \times 10^7$ N/m and $c_{yy} = 2{\cdot}65 \times 10^2$ N/m/s. All other parameters remain the same. Consider an unbalanced mass of $m_u e = 1{\cdot}0$ kg . m at node z_7. In Figure 12, the $A_m - \Omega$ curve of the rotor system at z_7 gives the first five critical speeds: 454, 777, 1032, 1254 and 1381. By equations (42), it is found that the first, third and fifth critical speeds are backward speeds, and the second and fourth forward ones.

The whirl orbits of the unbalanced rotor system at node z_7 are plotted in Figures 13 and 14, for five different types of Bearing 2 listed in Table 5. In all the cases, the rotation speeds are chosen as $\Omega_1 = 1000$ rad/s $= 9549$ r.p.m. and $\Omega_2 = 1{\cdot}5\Omega_1$. Except for the rotation speeds and the coefficients of Bearing 2, all the other parameters of the rotor system are the same as given in Table 3. The orbit in Case 1 is a circle due to the symmetry of the

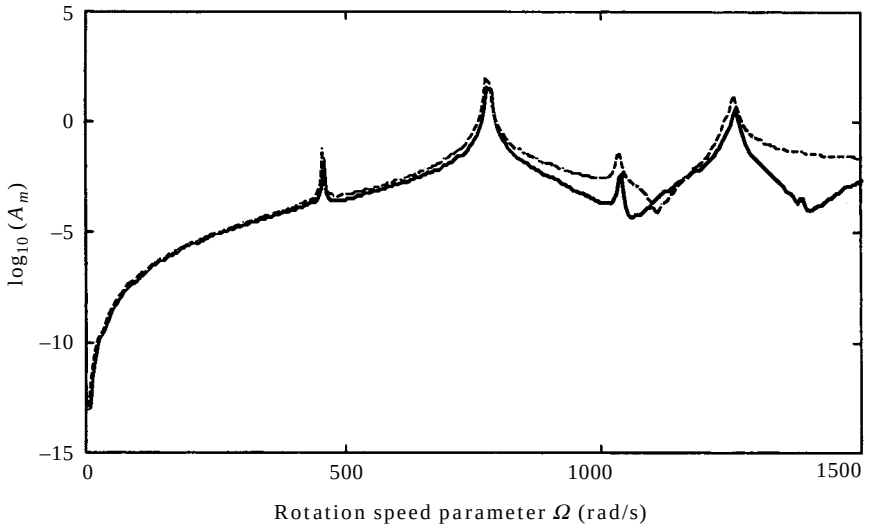

Figure 12. Amplitude of frequency response of the unsymmetric dual rotor system: ——, at Disk 2; - - - -, at Disk 4.

rotor system. Because $k_{xx} \neq k_{yy}$ and $c_{xx} \neq c_{yy}$ in Cases 2 and 3, the orbits become elliptic; see Figure 13. With the non-zero k_{xy}, k_{yx}, c_{xy} and c_{yx} in Cases 4 and 5, the whirl orbits not only are elliptic, but also become flat with their long axes titling from the x- or y-axis; see Figure 14. Moreover, by equations (42), the whirling in Case 1 is forward, and that in the rest of the cases is backward. Thus, an unsymmetric bearing can greatly affect the whirl direction and orbit of a complex rotor system.

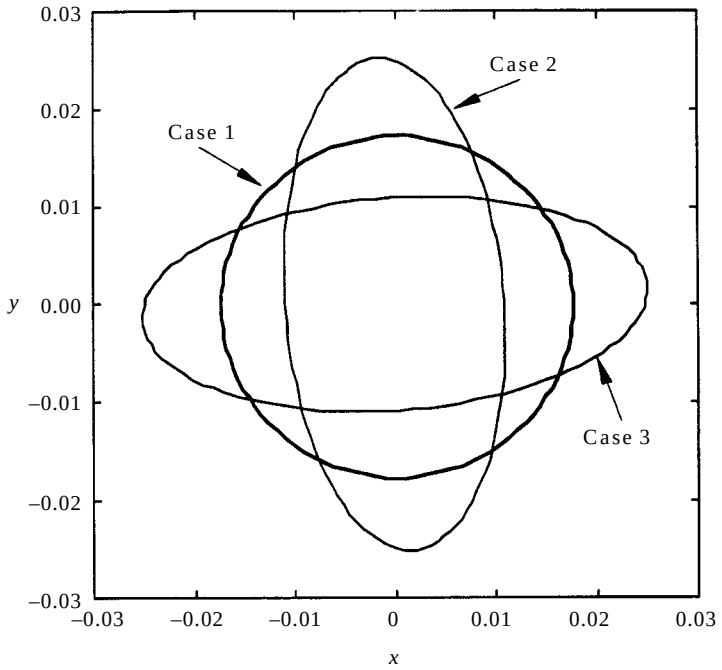

Figure 13. Whirl orbits of the unbalanced dual rotor system at node z_7: Cases 1, 2 and 3.

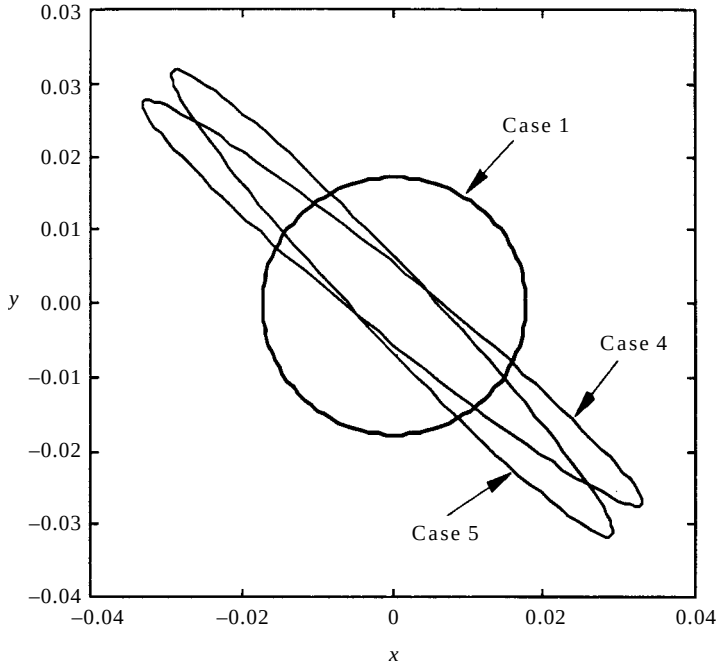

Figure 14. Whirl orbits of the unbalanced dual rotor system at node z_7: Cases 1, 4 and 5.

6. CONCLUSIONS

For a large class of complex rotor systems, the DTFS gives exact and closed-form predictions of dynamic displacements and stresses at any location. The method is capable of modelling flexible–rigid body interactions, and the combined effects of elastic deformations (bending, shear, torsional and longitudinal), rotary inertia, unbalanced masses, gyroscopic forces, and non-proportional damping due to bearings. The proposd method does not require a knowledge of comparison or admissible functions. Neither does it need specific derivations for different shaft models and boundary conditions. By treating different distributed and lumped components in a compact and unified form, the

TABLE 5

The coefficients of Bearing 2 (k_{xx}, *etc. in* N/m; c_{xx}, *etc. in* $N/m/s$)

Case no.	Coefficients of Bearing 2
1	The same as listed in Table 3
2	$k_{xx} = 1{\cdot}75 \times 10^7$, $k_{yy} = 2{\cdot}65 \times 10^7$, $k_{xy} = k_{yx} = 0$ $c_{xx} = 1{\cdot}75 \times 10^2$, $c_{yy} = 2{\cdot}65 \times 10^2$, $c_{xy} = c_{yx} = 0$
3	$k_{xx} = 2{\cdot}65 \times 10^7$, $k_{yy} = 1{\cdot}75 \times 10^7$, $k_{xy} = k_{yx} = 0$ $c_{xx} = 2{\cdot}65 \times 10^2$, $c_{yy} = 1{\cdot}75 \times 10^2$, $c_{xy} = c_{yx} = 0$
4	k_{xx}, k_{yy}, c_{xx} and c_{yy} are the same as in Case 1 $k_{xy} = 2{\cdot}65 \times 10^7$, $k_{yx} = 1{\cdot}75 \times 10^7$, $c_{xy} = 2{\cdot}65 \times 10^2$, $c_{yx} = 1{\cdot}75 \times 10^2$
5	k_{xx}, k_{yy}, c_{xx} and c_{yy} are the same as in Case 1 $k_{xy} = 1{\cdot}75 \times 10^7$, $k_{yx} = 2{\cdot}65 \times 10^7$, $c_{xy} = 1{\cdot}75 \times 10^2$, $c_{yx} = 2{\cdot}65 \times 10^2$

DTFS provides a new symbolic manipulation for real engineering analysis. The accuracy and efficiency of the method has been verified in the examples.

Some observations from the numerical simulation are as follows. In estimating critical speeds, a tapered flexible rotor can be accurately modelled by a stepped rotating beam of a small number of segments. For a symmetric dual rotor system, an unbalanced mass can only excite forward whirls. However, an unsymmetric bearing can dramatically change the whirl direction and orbit of the rotor system. Additionally, if an external harmonic excitation is not purely forward, both forward and backward whirls can be excited. In this case, the backward and forward critical speeds of the dual rotor system are in an interlacing relation.

The DTFS can be extended to rotors carrying flexible disks. Such systems have other important industrial applications besides those mentioned in the introduction. Two examples are data storage (e.g., computer disk drives) and material processing (e.g., circular saws). A recent study [29] shows that the distributed transfer functions of flexible rotating disks can be obtained in a highly accurate semi-analytical form. Hence, with flexible rotating disks treated as distributed components, a DTFS-based analysis for such rotating systems can be similarly developed.

ACKNOWLEDGMENT

This work was partially supported by the US Army Research Office.

REFERENCES

1. F. M. Dimentberg 1961 *Flexural Vibrations of Rotating Shafts*. London: Butterworths.
2. R. L. Eshleman 1978 *Flexible Rotor Bearing Systems Dynamics*. New York: ASME Publications.
3. A. D. Dimarogonas and S. A. Paipeties 1983 *Analytical Methods in Rotor Dynamics*. New York: Applied Science Publishers.
4. M. Lalanne and G. Ferraris 1990 *Rotordynamics Prediction in Engineering*. New York: Wiley.
5. J. S. Rao 1991 *Rotor Dynamics*. New York: Wiley.
6. F. F. Ehrich 1992 *Handbook of Rotordynamics*. New York: McGraw-Hill.
7. C. W. Lee 1993 *Vibration Analysis of Rotors*. Dordrecht: Kluwer Academic Publishers.
8. E. Krämer 1993 *Dynamics of Rotors and Foundations*. Berlin: Springer.
9. H. P. Lee 1995 *Journal of Sound and Vibration* **181**, 169–177. Dynamic response of a rotating Timoshenko shaft subject to axial forces and moving loads.
10. K. B. Yim, S. T. Noah and J. M. Vance 1986 *ASME Journal of Applied Mechancs* **53**, 711–718. Effect of tangential torque on the dynamics of flexible rotors.
11. J. S. Yun and C. W. Lee 1993 *ASME DE-Vol*. **60**, 331–338. Dynamic analysis of flexible rotors subjected to torque and force.
12. D. A. Glasgow and H. D. Nelson 1980 *ASME Journal Machine Design* **102**, 185–193. Stability analysis of rotor-bearing system using component mode synthesis.
13. H. D. Nelson and J. M. McVaugh 1976 *ASME Journal of Engineering for Industry* **98**, 593–600. The dynamics of rotor-bearing systems using finite elements.
14. T. C. Gmür and J. D. Rodrigues 1991 *ASME Journal of Vibration and Acoustics* **113**, 482–493. Shaft finite elements for rotor dynamic analysis.
15. Y. Kang, Y. P. Shih and A. C. Lee 1992 *ASME Journal of Vibration and Acoustics* **114**, 194–208. Investigation on the steady-state response of asymmetric rotors.
16. T. C. Huang 1961 *ASME Journal of Applied Mechanics* **28**, 579–584. The effect of rotary inertia and of shear deformation on the frequency and normal mode equations of uniform beams with simple end conditions.
17. J.-W. Zu and R. P. S. Han 1992 *ASME Journal of Applied Mechanics* **59**, 197–204. Natural frequencies and normal modes of a spinning Timoshenko beam with general boundary conditions.

18. T. C. Huang and F. C. C. Huang 1967 *ASME Journal of Engineering for Industry* **89**, 713–718. On precession and critical speeds of two bearing machines with overhung weight.
19. R. L. Eshleman and R. A. Eubanks 1969 *ASME Journal of Engineering for Industry* **91**, 1180–1188. On the critical speeds of a continuous rotor.
20. C. W. Lee, R. Katz, A. G. Ulsoy and R. A. Scott 1988 *Journal of Sound and Vibration* **122**, 119–130. Modal analysis of a distributed parameter rotating shaft.
21. W. Kuang and C. A. Tan 1993, *ASME DE-Vol*. **60**, 219–227. Vibration of a rotating stepped beam by the distributed transfer function method.
22. A.-C. Lee, Y. Kang and Y. P. Shih 1991 *ASME Journal of Applied Mechanics* **58**, 776–783. A modified transfer matrix method for linear rotor-bearing systems.
23. A. G. Butkoviskiy 1983 *Structural Theory of Distributed Systems*. New York: Wiley.
24. B. Yang 1992 *Journal of Sound and Vibration* **156**, 425–443. Transfer functions of constrained/combined one-dimensional continuous dynamic systems.
25. B. Yang 1994 *ASME Journal of Applied Mechanics* **61**, 84–92. Distributed transfer function analysis of complex distributed systems.
26. H. Fang 1996 *PhD Dissertation*, *University of Southern California*. Modeling and analysis of one-dimensional complex distributed parameter systems by the distributed transfer function method.
27. B. Yang and C. A. Tan 1991 *ASME Journal of Applied Mechanics* **59**, 1009–1014. Transfer functions of one-dimensional distributed parameter systems.
28. B. Yang and H. Fang 1994 *ASME Journal of Vibration and Acoustics* **116**, 426–432. Transfer function formulation of non-uniformly distributed parameter systems.
29. B. Yang and J. Zhou 1997 *Journal of Sound and Vibration* **201**, 641–647. Strip distributed transfer function analysis of circular and sectorial plates.